PHYSICAL REVIEW B **91**, 115304 (2015)

Nonlinear pulse propagation in InAs/InP quantum dot optical amplifiers: Rabi oscillations in the presence of nonresonant nonlinearities

O. Karni,[1,*] A. K. Mishra,[1] G. Eisenstein,[1] and J. P. Reithmaier[2]

[1]*Electrical Engineering Department, Technion–Israel Institute of Technology, Haifa 32000, Israel*

[2]*Technische Physik, Institute of Nanostructure Technologies and Analytics, CINSaT, University of Kassel, 34132 Kassel, Germany*

(Received 29 September 2014; revised manuscript received 15 January 2015; published 9 March 2015)

We study the interplay between coherent light-matter interactions and nonresonant pulse propagation effects when ultrashort pulses propagate in room-temperature quantum dot (QD) semiconductor optical amplifiers (SOAs). The signatures observed on a pulse envelope after propagating in a transparent SOA, when coherent Rabi oscillations are absent, highlight the contribution of two-photon absorption (TPA), and its accompanying Kerr-like effect, as well as of linear dispersion, to the modification of the pulse complex electric field profile. These effects are incorporated into our previously developed finite-difference time-domain comprehensive model that describes the interaction between the pulses and the QD SOA. The present generalized model is used to investigate the combined effect of coherent and nonresonant phenomena in the gain and absorption regimes of the QD SOA. It confirms that in the QD SOA we examined, linear dispersion in the presence of the Kerr-like effect causes pulse compression, which counteracts the pulse peak suppression due to TPA, and also modifies the patterns which the coherent Rabi oscillations imprint on the pulse envelope under both gain and absorption conditions. The inclusion of these effects leads to a better fit with experiments and to a better understanding of the interplay among the various mechanisms so as to be able to better analyze more complex future experiments of coherent light-matter interaction induced by short pulses propagating along an SOA.

DOI: 10.1103/PhysRevB.91.115304 PACS number(s): 78.20.Bh, 78.67.Hc, 42.65.Re, 79.20.Ws

I. INTRODUCTION

Active optical semiconductor waveguides, based on nanometric gain media including quantum dashes (QDashs) and quantum dots (QDs) have been extensively studied over the last decade to have a better understanding of their dynamical properties, and to explore possible applications in fast and efficient communication and processing systems. QDs have also been the focus of fundamental research, where quantum-mechanical phenomena are routinely exploited in these so-called "artificial atoms," usually at cryogenic temperatures. Recently, the two research domains were bridged, as coherent light-matter interactions have been demonstrated in electrically driven, room-temperature semiconductor optical amplifiers (SOAs) based on QDashs operating at 1.55 μm wavelength [1] and later also in QD SOAs operating at 1.55 μm [2] and at 1.3 μm [3].

These coherent observations were made possible using ultrafast techniques that can measure the complex envelope of an ultrashort light pulse after it had propagated through the waveguide of the SOA. The temporal width of the short pulses defined an interaction time shorter than the decoherence time of the medium, while the observation techniques provided the temporal resolution to observe details on time scales shorter than the pulses themselves. The experimental findings were also supported by numerical calculations accounting for the interaction of an electromagnetic pulse with an active waveguide, approximated as a cascade of semiclassical two-level systems in a similar manner as in Ref. [4], with the addition of slower, incoherent, charge carriers dynamics governed by a set of rate equations. A cascade of homogeneously broadened two-level systems [5] was first modeled, followed by an expansion to inhomogeneous ensembles of such two-level systems [2] in a later version. These comprehensive models were crucial for understanding how the coherent Rabi oscillations, which the medium undergoes during its interaction with the light pulses, imprint their signatures on the envelopes of the propagating pulses, resulting in the temporal amplitude and phase profiles evident at the output of the device. These models enabled one to identify qualitatively that coherent light-matter interactions were indeed responsible for the observed pulse shapes. However, they did not account for any other propagation phenomena, i.e., dispersion, two-photon absorption (TPA), and the Kerr effect, and hence were somewhat inaccurate with respect to a few of the details of the observed signatures.

Nonresonant propagation effects were frequently observed in dynamical experiments when pulses propagated through semiconductor optical waveguides. Pump-probe experiments with QDash SOAs at 1.5 μm [6,7] and at 1 μm [8] as well as 1.5 μm [9] QD SOAs revealed that an intense pump pulse injects charge carriers into the active region of the amplifier by TPA, and induces an increase in the gain which is experienced by a probe signal at the wavelength of the pump or any other wavelength within the gain spectrum. Since TPA absorbs the pulse peak more than its wings, it was also considered to be responsible for suppressing the pulse narrowing expected in self-induced transparency (SIT) [1].

Zilkie *et al.* showed that the TPA process is accompanied by a Kerr-like effect and produces an instantaneously appearing negative line-enhancement factor in QD SOAs when biased to absorption [10]. A similar Kerr-like effect in a bulk semiconductor was reported by Siederdissen *et al.* to cause self-phase modulation, and to create "soliton-like" pulse shapes, in combination with the linear dispersion [11]. Linear dispersion alone was measured, for example, in a QD SOA at 1.3 μm [12]. Romstad *et al.* have also demonstrated a complicated scenario for pulse propagation in bulk SOAs under

*oulrik@tx.technion.ac.il

different operating regimes involving nonresonant effects and nonadiabatic following [13], which called for further study to discriminate between their contributions. This was followed by a microscopic model for pulse-envelope propagation in bulk semiconductor [14,15], and a similar model was also reported for quantum well SOAs [16]. However, none of these studies treated theoretically the nonresonant propagation mechanisms. Thus, the ability to discriminate these effects from the coherent Rabi oscillations, by utilizing a wave-propagation numerical model, remained of great importance.

This paper reports such an investigation for QD SOAs operating at 1.55 μm, which was conducted in two steps. First, we experimentally characterized, by cross frequency resolved optical gating (XFROG) [17], the pulse envelope at the output of a QD SOA when biased to its resonant transparency. In this regime, the coherent interactions were diminished, and any signature imprinted on the pulse was solely due to the nonresonant mechanisms, allowing their separate study. In the second step, we enhanced our numerical model, to evaluate the effects of TPA, its accompanying Kerr-like effect, and linear dispersion in addition to the coherent light-matter interactions. This model is based on a finite-difference time-domain (FDTD) algorithm avoiding any slowly varying envelope approximations, and therefore allows one to investigate extremely fast dynamics, shorter than an optical cycle. It enables one to analyze the comprehensive response of the SOA alongside the pulse propagation in both the gain and absorption regimes of operation, allowing a separate investigation of the action of each of the mechanisms involved in shaping the pulse.

We found that in the transparency regime, the pulse experiences nonresonant absorption, as expected, and exhibits an instantaneous frequency profile which has the characteristics of a Kerr-like effect. For low intensities, the pulse showed a different, almost linear, chirp, which is dominated by linear dispersion. At sufficiently high energies, pulse narrowing was observed, indicating a soliton-like behavior. Using the enhanced numerical model, we also showed that the Kerr-like effect is crucial for the modeling of the experimentally observed signatures in both the gain and absorption regimes.

This paper is organized as follows. First, the experimental study of pulse propagation in a transparent QD SOA is presented in Sec. II. The numerical model is introduced in Sec. III, and Sec. IV presents the predictions of the model in the different operational regimes, and compares them with experimental results. Finally, Sec. V is devoted to conclusions.

II. PULSE PROPAGATION AT TRANSPARENCY

In order to discriminate experimentally between the signature of Rabi oscillations and nonresonant propagation phenomena, we characterized the envelope of a 185 fs wide pulse after propagation through the QD SOA waveguide, when biased to transparency. In transparency, the probabilities for resonant absorption and for stimulated emission are almost equal, and hence the pulse does not induce any modification to the charge carriers populations in the QDs, and no Rabi flopping takes place. Only nonresonant effects, such as dispersion, TPA, and its accompanying Kerr-like effect, can have a pronounced

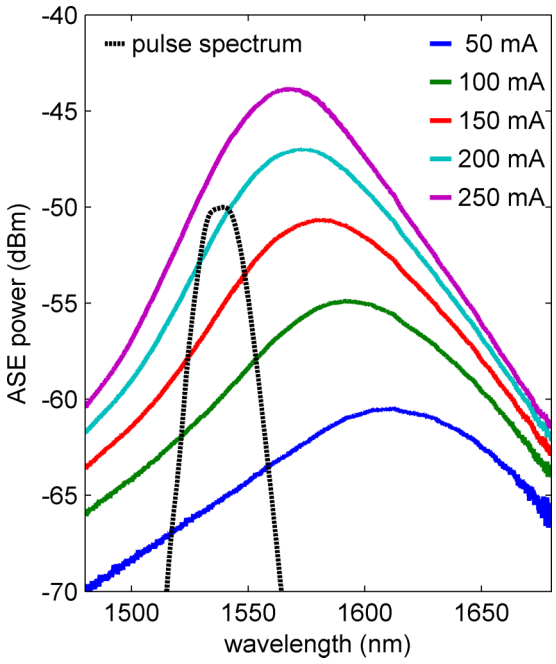

FIG. 1. (Color online) Bias-dependent emission spectra of the SOA, together with the spectrum of the excitation pulse used in the experiments.

signature. Thus, it is possible to identify their imprints on the pulse envelope separately from the coherent phenomena.

The device we examined was a 1.5 mm long edge emitting SOA comprising four layers of self-assembled InAs QDs placed between InGaAlAs barriers, grown on an InP substrate [18]. The bias-dependent amplified spontaneous emission spectra are shown in Fig. 1, exhibiting a 70 nm wide inhomogeneously broadened gain spectrum. The excitation pulses were filtered from the output of a Toptica FemtoFiber Pro fiber laser, with a maximum pulse energy of about 250 pJ (coupled to the SOA). The spectral shape of the excitation pulse is also shown in Fig. 1, exhibiting a bandwidth of about 20 nm [full width at half maximum (FWHM)] centered at 1540 nm. Thus, and because of the inhomogeneous gain broadening, the true transparency was only approximately achieved, as some parts of the pulse spectrum always experienced some absorption or amplification. Nonetheless, transparency was defined at the bias level where the effects of stimulated emission and absorption were minimal, by a simple single-wavelength pulsed pump-probe experiment. A bias of approximately 95 mA was found to be the transparency point since at this level the transmission of the probe pulse was not affected by the presence of the pump pulse, preceding it by a few hundreds of femtoseconds.

Next, we used the XFROG system to analyze the modifications induced on the pulse complex envelope in the above transparency point, for various input pulse energies. The results are summarized in Figs. 2(a) and 2(b), showing the temporal intensity and instantaneous frequency (chirp) profiles, respectively.

The measured intensity profiles show that as the input energy increases, the output pulses peaks become asymmetric and delayed. The peak intensities fail to follow the increase in

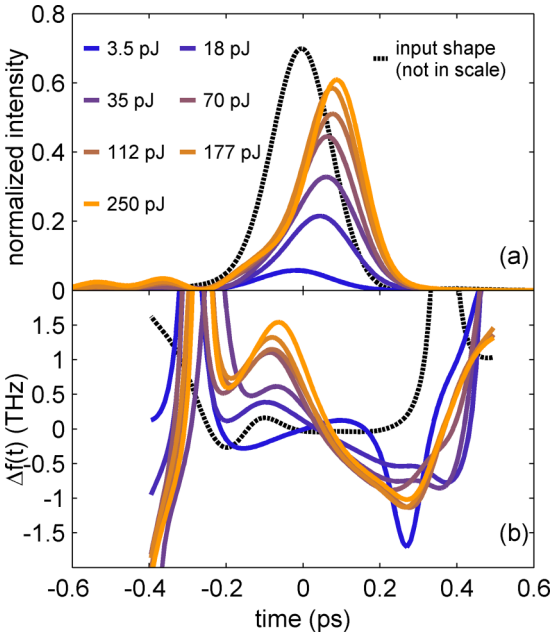

FIG. 2. (Color online) Transparency regime. (a) Measured time-dependent intensity profiles of the output pulses for various input energies. (b) Instantaneous frequency profile of the output pulses. The dashed curve presents the input pulse profiles. Its intensity is not plotted on the same scale as the output pulses.

the input energy, as also clearly presented in Fig. 3(a) (blue dots). Since the pulses are not broadened at the same time, this trend of the peak intensity indicates that the pulses experience an intensity-dependent absorption upon propagation along the waveguide.

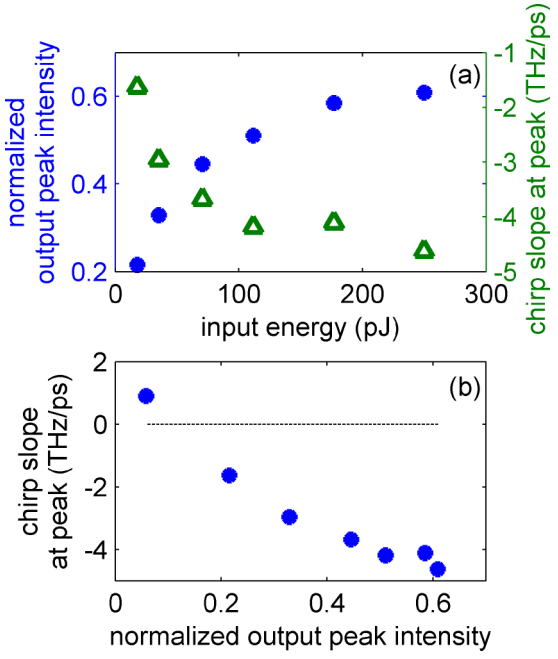

FIG. 3. (Color online) Transparency regime. (a) Normalized peak intensity at the output of the waveguide (blue dots), and chirp slope (green triangles) as a function of the pulse energy at the input. (b) Chirp slope as a function of the normalized output peak intensity.

The measured chirp profiles reveal a transition between two regimes. For a powerful, 250 pJ, input pulse, where the output intensity profile is the most augmented one in Fig. 2(a), the chirp profile shows a steep instantaneous frequency decrease. As the input energy is lowered, this chirp slope decreases (in its absolute value), down to a point where for the weak, 3.5 pJ, pulse, it exhibits a positive slope. The trend of the negative chirp slope with the input energy resembled that of the output peak intensity with the input energy as shown in Fig. 3(a) (green triangles). However, when plotted against the output peak intensity, the chirp slope changes almost linearly, as seen in Fig. 3(b). This trend implies an instantaneous, intensity-dependent phase modulation, namely, a Kerr-like effect. The presence of such a phenomenon has been reported in several past cases [10,11] in the context of TPA. Hence, we conclude that the observed effects are due to TPA (responsible for the intensity-dependent absorption) with an accompanying Kerr-like effect.

As the pulse intensity is reduced, these effects decay, and modifications to the pulse are dominated by linear dispersion, which creates the positive chirp slope. Opposite signs of the chirp, caused by dispersion and the Kerr-like effect, imply that the pulse narrowing at high energies is in fact a manifestation of "soliton-like" propagation, similar to the one reported in Ref. [11].

Thus, the experiments in the transparency regime highlight the significance of TPA, its accompanying Kerr-like effect, and of the linear dispersion, in shaping the pulses which propagate in the SOA. Deciphering the combined effect of the various propagation effects and the coherent Rabi oscillations evident in higher or lower bias levels requires a proper model. Accordingly, such a comprehensive FDTD model that considers all these phenomena, and allows a thorough study of their collective signature, is introduced in the next section.

III. NUMERICAL MODEL

The proposed model solves Maxwell's equations governing the electromagnetic pulse propagation, where the response of the medium is expressed through the induced polarization term. Each phenomenon is therefore considered by its particular contribution to the induced polarization. We invoke a full-wave FDTD numerical algorithm that allows examination of the coevolution of the electromagnetic wave and any other fast dynamical mechanism, such as the evolution of a two-level system, without using any rotating-wave or slowly varying envelope approximations.

The present model extends our previous models of coherent light-matter interactions [2,5]. The electromagnetic field is assumed to propagate as a TEM mode along the Z axis of the amplifier, which in turn is modeled as a cascade of ensembles of quantum-mechanical two-level systems, expressing the inhomogeneous spectral broadening of the self-assembled QD medium. The dynamics of these two-level systems are treated by solving the Schrödinger equation in the density-matrix formalism. Each two-level system describes a ground state in a QD which is fed, incoherently, with charge carriers from an excited state belonging to the same QD. Charge carriers are captured in, or escape out of these QDs to a carrier reservoir residing at higher energy levels, which is fed by

the external current supply. All these incoherent dynamics are evaluated using a set of rate equations. Technically speaking, Maxwell's and Schrödinger's equations are treated with a central difference discretization, and the slower rate equations are propagated with a forward difference discretization.

The calculation of pulse propagation is established, as already mentioned, on the solution of Maxwell's curl equations, for an electric field polarized along the X axis, and a magnetic field pointing in the Y direction,

$$\frac{\partial E_x}{\partial z} = -\mu_0 \frac{\partial H_y}{\partial t}, \quad -\frac{\partial H_y}{\partial z} = \frac{\partial D_x}{\partial t}, \tag{1}$$

where E_x, D_x, and H_y are the electric field, electric displacement, and magnetic field components, respectively, and μ_0 is the permeability of the vacuum. The displacement is related to the electric field and to the induced polarization P_x,

$$D_x = \varepsilon_0 \varepsilon_\infty E_x + P_x, \tag{2}$$

with ε_0 being the permittivity of the vacuum, and ε_∞ is the dielectric constant for an infinite frequency. In every time step of the FDTD algorithm, Eq. (1) is evaluated to provide the values for H_y and D_x along the amplifier. These are used to calculate the various polarization elements, which in turn enable one to calculate E_x based on Eq. (2), and proceed to the next time step.

The polarization P_x comprises several contributions:

$$P_x = P_{\text{dispersion}} + P_{\text{Kerr}} + P_{\text{TPA}} + P_{\text{QD}} + P_{\text{plasma}}. \tag{3}$$

$P_{\text{dispersion}}$ accounts for the linear (with the field) contribution. P_{TPA} and P_{Kerr} represent the contributions of the TPA of the wave and of the accompanying Kerr-like effect, respectively. The interaction with the QDs and their charge carriers is folded in P_{QD} and P_{plasma}, determining the radiation of the two-level systems, and the changes in refractive index due to the carrier population at the various energy levels.

The linear dispersion is introduced phenomenologically by driving a lossless Lorentz oscillator [19,20], avoiding frequency-dependent absorption arising from this contribution:

$$\frac{\partial^2 P_{\text{dispersion}}}{\partial t^2} + \omega_L^2 P_{\text{dispersion}} = \varepsilon_0 \chi_L \omega_L^2 E_x. \tag{4}$$

Here, ω_L is the resonant frequency of the Lorentz oscillator, and χ_L is the oscillator strength. Both serve to determine the desired refractive index and the desired degree of group velocity dispersion (GVD). This is performed by transforming (4) to the frequency domain, obtaining

$$P_{\text{dispersion}}(\omega) = \frac{\varepsilon_0 \chi_L \omega_L^2 E_x}{\left(\omega_L^2 - \omega^2\right)}. \tag{5}$$

Hence, the nominal dielectric constant at the central excitation frequency ω is given by (including the response of the medium at infinite frequency ε_∞)

$$\varepsilon(\omega) = \varepsilon_\infty + \frac{\chi_L \omega_L^2}{\omega_L^2 - \omega^2}. \tag{6}$$

The GVD is then expressed by the second derivative, with respect to ω, of the propagation coefficient $\beta(\omega) = \frac{\omega}{c}\sqrt{\varepsilon(\omega)}$ (c is the speed of light in vacuum). Choosing a nominal dielectric constant of 12.25, representing this property of semiconductors at optical frequencies [21], and fixing the GVD to a desired positive value, one is able to solve for the parameters (χ_L, ω_L) of the Lorentz oscillator. Then, the dynamics of this oscillator are evaluated in each time step of the calculation process, using the known values of the field variables $P_{\text{dispersion}}$ and D_x, according to the following discretization scheme [19]:

$$\begin{aligned} &\frac{P_{\text{dispersion}}^{n+1} - 2P_{\text{dispersion}}^{n} + P_{\text{dispersion}}^{n-1}}{\Delta t^2} \\ &\quad + \frac{\omega_L^2\left(P_{\text{dispersion}}^{n+1} + P_{\text{dispersion}}^{n-1}\right)}{2} \\ &\quad = \frac{\omega_L^2 \chi_L \left(D^{n+1} + D^{n-1} - P_{\text{dispersion}}^{n+1} - P_{\text{dispersion}}^{n-1}\right)}{2\varepsilon_\infty}. \end{aligned} \tag{7}$$

Δt is the time increment used in the simulation, and the superscripts $n-1$, n, and $n+1$ denote the previous time step, the current time, and the next time step, respectively. If negative GVD values are needed, a Drude model can similarly be applied instead of the Lorentz oscillator.

The treatment of the nonlinear terms starts by formulating the relation between the TPA susceptibility and the strength of the Kerr effect, in an α-factor relation, which is described in the frequency domain by

$$P_{\text{TPA+Kerr}}(\omega) = \varepsilon_0 (1 + j\alpha_{\text{TPA}}) \chi_{\text{TPA}} E_x(\omega), \tag{8}$$

where $j = \sqrt{-1}$, and α_{TPA} is the factor relating the effect of TPA on the refractive index to its effect on the amplitude of the wave [10]. χ_{TPA} is the TPA susceptibility. In the frequency domain, it is related to the TPA efficiency β_{TPA} (defined by Beer's law for the light intensity, $\frac{\partial I}{\partial z} = -\beta_{\text{TPA}} I^2$) by [20]

$$\chi_{\text{TPA}} = \frac{c^2 \varepsilon_0 n_0^2 \beta_{\text{TPA}}}{2j\omega} |E_x|^2, \tag{9}$$

with n_0 being the nominal refractive index. The TPA polarization is thus imaginary, while the Kerr effect polarization is real, therefore different treatments are required to fit them into the FDTD simulator that deals with real polarizations only. The Kerr effect simply modifies the refractive index of the medium, and its induced polarization is real, formulated as [20]

$$P_{\text{Kerr}} = \varepsilon_0 \frac{\alpha_{\text{TPA}} \varepsilon_0 c^2 n_0^2 \beta_{\text{TPA}} |E_x|^2}{2\omega} E_x. \tag{10}$$

This is calculated at the central frequency of the wave. In principle, more complicated effects such as self-steepening may be considered. In that case, the Kerr polarization must include an independent dynamics driven by the wave [20], in a similar fashion to what has been used for the case of linear dispersion. These complications have been avoided in the present model.

Owing to its specific imaginary character in the frequency domain, the contribution of the TPA in the time domain is considered after performing a time derivative of Eq. (2) [20],

$$\begin{aligned} \frac{\partial D_x}{\partial t} &= \varepsilon_0 \varepsilon_\infty \frac{\partial E_x}{\partial t} + \frac{\partial P_{\text{dispersion}}}{\partial t} + \frac{\partial P_{\text{Kerr}}}{\partial t} \\ &\quad + \frac{\partial P_{\text{QD}}}{\partial t} + \frac{\partial P_{\text{plasma}}}{\partial t} + \tilde{P}_{\text{TPA}}, \end{aligned} \tag{11}$$

where

$$\tilde{P}_{\mathrm{TPA}} = \frac{c^2\varepsilon_0^2 n_0^2 \beta_{\mathrm{TPA}} |E_x|^2}{2} E_x. \tag{12}$$

The polarization contributed by the two-level systems is calculated from the coherence terms in their density matrices [5]. The dynamic behavior is obtained from the dynamics of Schrödinger's equation. Although it affects the wave amplitude, it is a real polarization term, and therefore it too was derived with respect to time in (11).

Finally, the contribution of the plasma effect is dealt with by introducing the proper polarization contribution, considering the modifications made to the dielectric constant in the medium:

$$P_{\mathrm{plasma}} = \varepsilon_0 \Delta\varepsilon_{\mathrm{plasma}} E. \tag{13}$$

This change is defined phenomenologically by the population of charge carriers in all the energy levels,

$$\Delta\varepsilon = 2C_{11} \sum_{\mathrm{ensemble}} N_d^i \rho_{11}^i + 2\,C_{22} \sum_{\mathrm{ensemble}} N_d^i \rho_{22}^i + C_{\mathrm{ex}} \sum_{\mathrm{ensemble}} N_{\mathrm{ex}}^i + C_{\mathrm{res}} N_{\mathrm{res}} + C_{h_{\mathrm{res}}} h_{\mathrm{res}}, \tag{14}$$

where C_{res}, C_{ex}, C_{11}, C_{22}, and $C_{h_{\mathrm{res}}}$ are phenomenological coefficients describing the change in the dielectric constant due to carrier populations in the electron reservoir, excited states of the QDs, upper states (of the two-level systems), lower states, and the hole reservoir, respectively. In (14) these are multiplied respectively by the populations N_{res}, $\sum_{\mathrm{ensemble}} N_{\mathrm{ex}}^i$, $2\sum_{\mathrm{ensemble}} N_d^i \rho_{11}^i$, $2\sum_{\mathrm{ensemble}} N_d^i \rho_{22}^i$, and h_{res}, where summations are performed in order to account for the entire QD inhomogeneously broadened spectrum. N_d^i is the QD volume density for the ith subgroup of QDs, and ρ_{11}^i (ρ_{22}^i) is the population probability of the upper (lower) state in the corresponding two-level system. Adding this polarization to (11) yields

$$\frac{\partial D_x}{\partial t} = \varepsilon_0\varepsilon_\infty \frac{\partial E_x}{\partial t} + \frac{\partial P_{\mathrm{dispersion}}}{\partial t} + \frac{\partial P_{\mathrm{Kerr}}}{\partial t} + \frac{\partial P_{\mathrm{QD}}}{\partial t} + \varepsilon_0 \frac{\partial(\Delta\varepsilon_{\mathrm{plasma}} E_x)}{\partial t} + \tilde{P}_{\mathrm{TPA}}. \tag{15}$$

This relation is evaluated in each time step in order to calculate the electric field for the next step. The difference equation obtained by discretizing (15) is advanced iteratively [20].

Unlike the wave-propagation procedure, which was significantly altered from the previous models [2,5], the charge-carrier dynamics are only slightly modified so as to accommodate the additional charge carriers injected by TPA. It has been assumed that they are injected into a very high energy level with an infinite density of states, so that population inversion cannot occur there. From this level, the carriers relax to the electron or hole reservoirs, or recombine, obeying the following rate equations:

$$\begin{aligned} \frac{\partial N_{\mathrm{TPA}}}{\partial t} &= I_{\mathrm{TPA}} - \left(1 - \frac{N_{\mathrm{res}}}{D_{\mathrm{res}}}\right) \frac{N_{\mathrm{TPA}}}{\tau_{\mathrm{TPA_{relax}}}} - \frac{N_{\mathrm{TPA}}}{\tau_{\mathrm{TPA_{rec}}}}, \\ \frac{\partial h_{\mathrm{TPA}}}{\partial t} &= I_{\mathrm{TPA}} - \left(1 - \frac{h_{\mathrm{res}}}{D_{\mathrm{res}}}\right) \frac{1}{\tau_{h_{\mathrm{TPA_{relax}}}}} h_{\mathrm{TPA}} - \frac{N_{\mathrm{TPA}}}{\tau_{\mathrm{TPA_{rec}}}}. \end{aligned} \tag{16}$$

N_{TPA} and h_{TPA} are the electron and hole population in the TPA injection levels. D_{res} is the density of states in the carrier reservoirs which the injected carriers relax into, with the time constants $\tau_{\mathrm{TPA_{relax}}}$ and $\tau_{h_{\mathrm{TPA_{relax}}}}$, for the injected electrons and holes, respectively. $\tau_{\mathrm{TPA_{rec}}}$ is the time scale of direct recombination of the charge carriers in those levels. I_{TPA} is the generation rate of carriers by TPA. It is related to the light intensity I and to the electric field by [20]

$$I_{\mathrm{TPA}} = \frac{\beta_{\mathrm{TPA}}}{2\hbar\omega} I^2 = \frac{\beta_{\mathrm{TPA}} c^2 \varepsilon_0^2 n^2}{8\hbar\omega} |E_x|^4. \tag{17}$$

This concludes the introduction of our comprehensive numerical model.

IV. SIMULATION RESULTS AND DISCUSSION

The model described in Sec. III was used to examine the imprints of the combined effects of coherent light-matter interactions and nonresonant propagation phenomena on the envelope of a 185 fs wide, transform-limited pulse, launched at the input of the calculation space. Since many phenomenological parameters were involved, and due to the large computational complexities of the calculation process, the simulations served only to follow qualitatively the trends observed in the experiments. To that end, we modeled a shorter propagation length, with relatively strong parameters for the various mechanisms. The parameters which had to be tuned for the task were the bias level of the device, the pulse input energy, the GVD, TPA efficiency β_{TPA}, the Kerr-like parameter α_{TPA}, the dipole moments for the two-level systems, the overall density of QDs, and the various α parameters of the charge carriers populations. All these have a direct impact on the time scale of the pulse itself, and affect its reshaping. The dipole moment was tuned to obtain pulse areas of roughly 4π for the maximum considered pulse energy (800 pJ before coupling losses), which were implied by our previous experiments in the gain regime [2]. The QDs' density was fixed to a value that enabled one to observe their signature on the pulse shape, accumulated along the short waveguide we modeled. Other parameters which had a lesser effect on the pulse shape were kept constant throughout the investigation. Their values, following our previous experiences with similar models [1], are listed in Table I.

Reconstructing the different signatures on the pulse envelope required one to identify the simulation bias levels which corresponded to the bias points in the experiments, and then tuning the parameters governing the propagation and the carrier effects. This tuning followed a few guidelines in order to keep the model physically reasonable: TPA efficiency and its accompanying Kerr effect were fixed for all the bias points [10], the GVD value was allowed to change monotonically with the bias level [12,22], and the effect of carrier population on the refractive index of the medium was assumed to be stronger in the gain regime compared to the absorption regime [10].

The results of the calculations are described in the following sections, concentrating on operating at the transparency point, in the gain regime, and finally in absorption. In each section, the results are compared to experimental observations, and the origins of the various signatures are discussed.

TABLE I. List of the constant parameters used in the simulations.

Parameter	Value
1. Active region geometry	
a. Length (μm)	300
b. Width (μm)	4
c. Number of QD layers	5
d. Layer thickness (nm)	10
e. Confinement factor (%)	0.25
f. Nominal refractive index	3.5
2. Electromagnetic stimulus	
a. Central wavelength (nm)	1540
b. FWHM (fs)	185
3. Resonant gain medium	
a. Dipole moment (Cm)	0.8×10^{-28}
b. Peak wavelength (nm)	1580
c. Inhomogeneous broadening (nm)	70
d. Homogeneous broadening (nm)	25
e. Number of sublevels	44
4. Rate equations parameters	
a. Total QD density (m^{-3})	4×10^{23}
b. Carrier reservoirs' density of states (m^{-3})	2×10^{25}
c. Carrier reservoir wavelength (nm)	1450
d. Excited-ground state energy separation (nm)	50
e. Recombination times (ns)	0.4
f. Electron capture time into the QDs (ps)	1
g. Excited-ground state relaxation time (fs)	100
h. Hole capture time into the QDs (fs)	100
i. Hole escape time from the QDs (fs)	100
j. Relaxation time of the TPA electrons (ps)	3
k. Relaxation time of the TPA holes (ps)	3

A. Transparency

Transparency point was identified in the model as the bias level in which the two-level systems in resonance with the pulse central wavelength had equal occupation probabilities in both their eigenstates, in the absence of any electromagnetic excitation. For the active region geometry, gain spectrum properties, and QD density listed in Table I, this was achieved at 42 mA. To provide a positive chirp slope for weak pulses, similar to what was observed for 3.5 pJ pulses (see Fig. 2), a positive GVD was assumed in the simulation. For more intense pulses, TPA truncated the pulses' peaks, effectively broadening them in time. However, the accompanying Kerr effect, which introduced a negative α_{TPA} value, created a positive chirp on the leading edge of the pulses, and a negative chirp on their trailing edges. Together with the dispersion, it acted to compress the pulses into a "soliton-like" structure. A proper balance between these effects was required for the reconstruction of the observed pulse narrowing. Furthermore, the coefficients of the carriers' plasma effect were introduced, keeping their values in the carrier reservoirs to be higher than those of the QD ground states. As a consequence, the carriers which were generated by TPA also contributed a chirp via the plasma effect. For positive α parameters, this effect resulted in a slight increase of the instantaneous frequency of the pulse along its trailing slope, effectively assisting the linear dispersion. The results, obtained with the parameters listed in

TABLE II. Simulation parameters for balancing GVD, TPA, the Kerr effect, and the plasma effect at the transparency bias of 42 mA.

Parameter	Value
1. Propagation effects	
a. β_{TPA} (GW/cm^2)	10
b. α_{TPA}	−2.5
c. GVD (fs^2/mm)	25 000
2. Plasma effect coefficients	
a. C_{res} (m^3)	0.1×10^{-26}
b. C_{ex} (m^3)	0.05×10^{-26}
c. C_{11} (m^3)	0.01×10^{-26}
d. C_{22} (m^3)	0.02×10^{-26}
e. $C_{h_{\mathrm{res}}}$ (m^3)	0.1×10^{-26}

Table II, for input pulse energies between 10 and 800 pJ, are plotted in Figs. 4(a) and 4(b), showing the time-dependent intensity and chirp profiles, respectively, of the output pulses. The inset of Fig. 4(a) presents the pulse widths (FWHM) as a function of their input energies (note the logarithmic scale of the energy axis). It shows that the weak pulses are broadened by dispersion, while the powerful pulses are compressed, as demonstrated experimentally. The intensity profiles in Fig. 4(a) demonstrate the effect of TPA in diminishing the pulse peak with respect to its initial energy, as it does not increase at the same rate as the input pulse intensity does. Figure 4(b) presents the evolution of the instantaneous frequency traces around the center of the pulse from the rising, dispersion dominated, profiles of the weak pulses, to the decreasing, Kerr effect dominated, profiles for the intense pulses. As

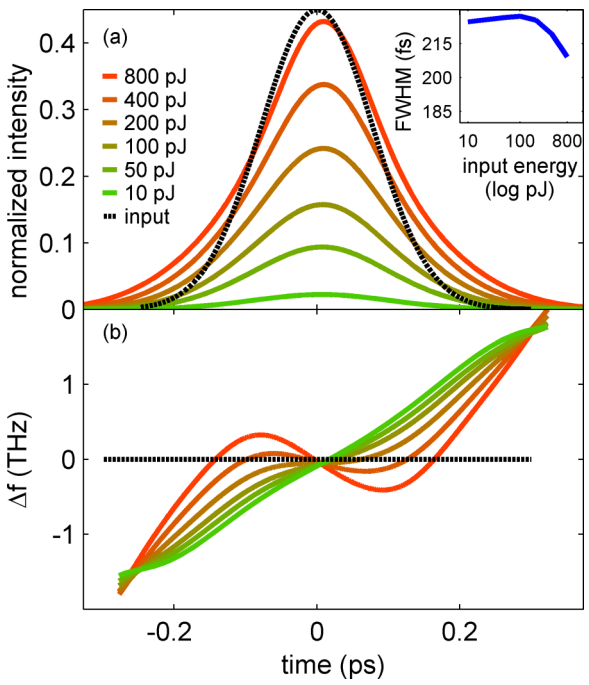

FIG. 4. (Color online) Pulse propagation at transparency. (a) Calculated output pulse time-dependent intensity for various input energies. Inset: Corresponding pulse widths vs input energy. (b) Corresponding calculated instantaneous frequency profiles.

the model assumes an ideal, transform limited, Gaussian pulse shape at the input, deviations from the exact measured profiles are evident. Nevertheless, it demonstrates the same qualitative trends observed in experiments, concluding that within the present computational limitations, this numerical apparatus mimics the physical mechanisms taking place.

B. Gain regime

In the next stage of the investigation, the effects of GVD, TPA, and its accompanying Kerr effect were studied in the gain regime (using a simulated bias of 100 mA), where coherent light-matter interactions are pronounced. At this bias level, the same pulses which were tested at transparency triggered up to two cycles of Rabi oscillations in the resonant two-level systems, in a similar fashion to our previous experimental observations. In order to clarify the role of these Rabi oscillations in shaping the pulse envelopes, as compared to the nonresonant effects, we considered two cases, one with and the second without the TPA and the accompanying Kerr effect contributions. The predicted output pulse shapes for various input energies, obtained using the parameters summarized in Table III, and compared with an experimental measurement of similar pulses which had propagated through the SOA under gain conditions, are plotted in Fig. 5. It presents the time-dependent intensity profiles of the predicted pulses without accounting for the TPA and Kerr effects [Fig. 5(a)], of the predicted pulses with these effects included [Fig. 5(c)], and of the experimental measurement [Fig. 5(e)]. Figures 5(b), 5(d), and 5(f) show the corresponding instantaneous frequency profiles, which are shifted vertically for clarity.

TABLE III. Simulation parameters for balancing GVD, TPA, the Kerr effect, and the plasma effect at 100 mA bias, availing the gain regime.

Parameter	Value
1. Propagation effects	
a. β_{TPA} (GW/cm^2)	10
b. α_{TPA}	−2.5
c. GVD (fs^2/mm)	2000
2. Plasma effect coefficients	
a. C_{res} (m^3)	0.15×10^{-26}
b. C_{ex} (m^3)	0.1×10^{-26}
c. C_{11} (m^3)	0.02×10^{-26}
d. C_{22} (m^3)	0.05×10^{-26}
e. $C_{h_{\mathrm{res}}}$ (m^3)	0.2×10^{-26}

In Figs. 5(a) and 5(b), the intensity and chirp profiles reveal the evolution of the oscillations imprinted by the coherent interaction with the two-level systems: Each Rabi cycle is accompanied by a temporary redshift, caused by the plasma effect of the charge carriers on the refractive index of the medium [1]. Thus, the chirp profiles reveal that the 100 pJ pulse has triggered a complete Rabi cycle, and a second one is starting. When the pulse intensity increases further, this second cycle advances, and the imprinted oscillations in the chirp become clear, and are also followed by a matching oscillation in the amplitude profiles, with multiple peaks corresponding to each of the redshifts. Moreover, as the pulse intensity rises, the first peak and the first redshift advance gradually to earlier times, consistent with the rise in the Rabi frequency. However,

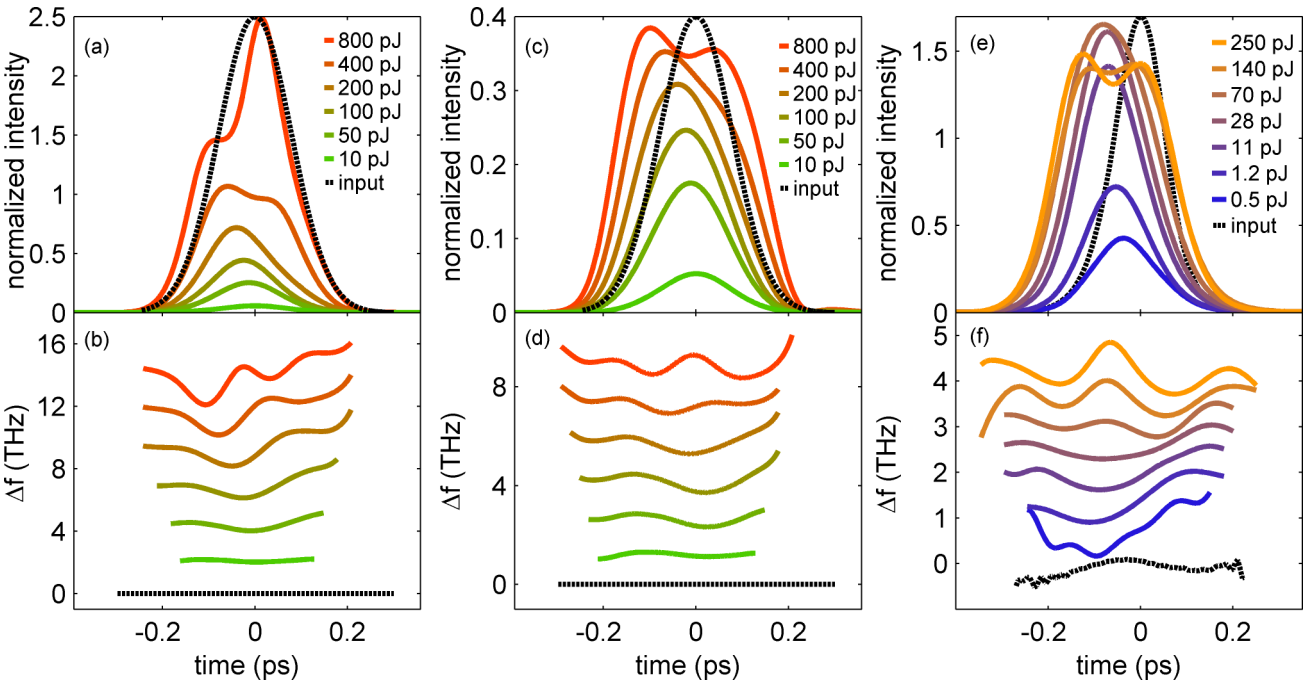

FIG. 5. (Color online) Pulse propagation in gain regime. (a) Calculated time-dependent intensity of the output pulses, not accounting for TPA and the Kerr effect. (b) The corresponding instantaneous frequency patterns. (c) Calculated time-dependent intensity of the output pulses, including TPA and the Kerr effect. (d) The corresponding instantaneous frequency patterns. (e) Measured time-dependent intensity of the output pulses from the real SOA. (f) The corresponding instantaneous frequency patterns.

the pattern visible in the instantaneous frequency plots is significant only along the first Rabi cycle, which is explained as follows. The fast carrier replenishment into the QDs from the carrier reservoir causes depletion of the reservoir. Since the plasma effect of the reservoir is strong, it creates a pronounced redshift on the leading edge of the pulse. On the other hand, this relaxation quickly averages out the population oscillations in the carrier reservoir, and so the second Rabi cycle is manifested by a minor redshift in the chirp profile, as the population of the QDs affects the chirp much less than that the reservoir.

Introducing the TPA and its accompanying Kerr effect, while keeping the other parameters fixed, resulted in the evolution presented in Figs. 5(c) and 5(d). Similar to the case of transparency, the TPA itself suppresses and clamps the peak intensities of the high energy pulses. The pulse areas are effectively reduced, and their coherent interactions with the two-level systems are weakened, preventing the appearance of the second Rabi-cycle signature at the moderate energies, whose absence is sensed when comparing Figs. 5(d) and 5(b) for the 100 and 200 pJ cases, for example. Nevertheless, Fig. 5(c) still shows clearly the intensity oscillations due to the coherent interaction, when the pulse intensity is sufficiently high. The Kerr effect acts to raise the instantaneous frequency whenever the pulse intensity rises, and to lower it when the pulse intensity reduces. Together with the linear dispersion, this effect balances the chirp induced by the charge carriers, and also slightly compresses the pulse lobes, bringing them closer together. Thus, the overall evolution of the pulse envelope is milder compared with the case without TPA. When the pulse area is sufficiently high, it splits into two lobes, which drift apart considerably and produce two corresponding redshifts which are of similar depths, as demonstrated in Fig. 5(d). The pulse envelopes, measured at the output of the QD SOA under a bias of 250 mA, are shown in Figs. 5(e) and 5(f). The figures exhibit a qualitatively similar evolution. The oscillations in the intensity profile [Fig. 5(e)] do not grow gradually but rather appear as the input pulse energy crosses a certain value. The peak intensity is clamped, especially when the input intensity produces the coherent oscillations. This severe clamping is consistent with our predictions, shown in Fig. 5(c), where the coherent transition along the pulse from stimulated emission to absorption adds to the truncation of the pulse peak by TPA. In contrast, this feature is not sensed at all in the reduced model without TPA. The corresponding chirp profile, in Fig. 5(f), also presents mild features, with a single redshift feature, turning, upon crossing the coherent breakup "threshold," into two similar valued redshifts, which are torn apart from each other. We therefore conclude that in gain regime, the model that combines the coherent Rabi oscillations and the nonresonant effects improves the predictions of the pulse shapes at the SOA output, and enables one to discriminate among the contributions from each of the mechanisms.

C. Absorption regime

Finally, absorption conditions were modeled by applying a 10 mA bias, and the nonresonant parameters listed in Table IV. Here again, the results of the full model were compared to a calculation ignoring the TPA and the Kerr effect, and to an experimental measurement. The comparisons are depicted in Fig. 6, which present the time-dependent intensity profiles of the predicted pulses without accounting for the TPA and Kerr effects [Fig. 6(a)], of the predicted pulses with these effects included [Fig. 6(c)], and of the experimental measurement [Fig. 6(e)]. Figures 6(b), 6(d), and 6(f) show the corresponding instantaneous frequency profiles, which are shifted vertically for clarity. The insets in the intensity profiles present the pulse widths (FWHM) as function of the input pulse energy.

TABLE IV. Simulation parameters for balancing GVD, TPA, the Kerr effect, and the plasma effect at 10 mA bias, availing the absorption regime.

Parameter	Value
1. Propagation effects	
a. β_{TPA} (GW/cm^2)	10
b. α_{TPA}	−2.5
c. GVD (fs^2/mm)	25 000
2. Plasma effect coefficients	
a. C_{res} (m^3)	0.1×10^{-26}
b. C_{ex} (m^3)	0.05×10^{-26}
c. C_{11} (m^3)	0.01×10^{-26}
d. C_{22} (m^3)	0.02×10^{-26}
e. $C_{h_{\mathrm{res}}}$ (m^3)	0.1×10^{-26}

Since the pulses are absorbed, their areas are in general diminished so that the common shape of their intensity profiles has a single peak, without any oscillations. Some pulse compression is measured as the input energy is raised [Fig. 6(e)]. This trend is reconstructed in our models, as emphasized by the insets of Figs. 6(a) and 6(c), but as the energy is further raised in the model without TPA, the FWHM of the output pulse starts to increase. This effect was not observed in the measurements, thus highlighting the need to account for TPA when modeling the experiments. Another difference between the predictions of the two models is in the peak intensity of the pulses, which are quenched by TPA.

The instantaneous frequency profiles, however, provide a more powerful evidence for the role of the nonresonant effects. The calculations which disregard TPA predict that the absorption of the pulse, generating charge carriers in the SOA, induces a positive chirp along the leading edge of the pulse, seen in Fig. 6(b). Even for intense pulses, which trigger coherent self-induced transparency (SIT), the chirp is mainly positive, again due to the fast escape of charge carriers from the two-level systems. The introduction of the TPA with its accompanying Kerr effect creates a mechanism that induces a negative effect on the chirp profile [10]. It induces the temporal decrease in the instantaneous frequency shown in Fig. 6(d). Since this chirp is opposite to that induced by the linear dispersion of the medium, it also leads to some pulse compression.

This redshift is clearly evident in the experimental findings in Fig. 6(f), and therefore further confirms the need to include TPA and the Kerr effect in the model. The observed compression of the intensity profile for 250 pJ input energy [Fig. 6(e)] is explained by the SIT mechanism assisted by the focusing action of the Kerr-like effect and the dispersion.

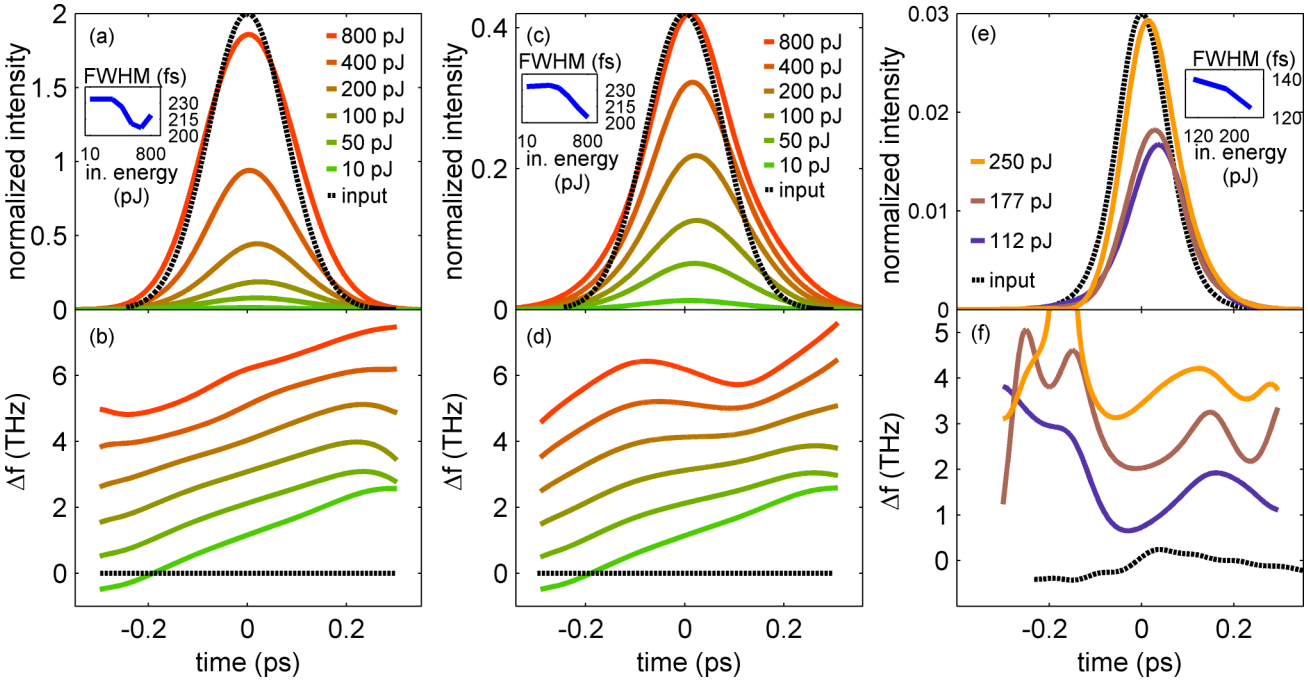

FIG. 6. (Color online) Pulse propagation in absorption regime. (a) Calculated time-dependent intensity of the output pulses, not accounting for TPA and the Kerr effect. (b) The corresponding instantaneous frequency patterns. (c) Calculated time-dependent intensity of the output pulses, including TPA and the Kerr effect. (d) The corresponding instantaneous frequency patterns. (e) Measured time-dependent intensity of the output pulses from the real SOA. (f) The corresponding instantaneous frequency patterns. The insets show the FWHM values vs input energy regarding each of the three cases.

V. CONCLUSION

In conclusion, we studied the impact of nonresonant propagation effects on the envelope of an ultrashort pulse as it propagates through a QD SOA and experiences coherent light-matter interactions such as Rabi oscillations.

XFROG characterization of the pulse complex envelope at the output of the SOA under transparency conditions (where the coherent interactions are diminished) revealed that linear dispersion, TPA, and a Kerr-like effect contribute significantly in shaping the pulse envelope. In order to discriminate these effects in the gain and absorption regimes as well, a comprehensive numerical model describing the pulse propagation was developed. This model integrates our previously developed FDTD numerical simulation tools describing the propagation of a pulse through a chain of quantum-mechanical two-level systems with additional FDTD schemes that model the nonresonant propagation effects of TPA, Kerr, and GVD. The model reconstructed qualitatively the pulse shapes and their evolution with the pulse input intensity at transparency, gain, and absorption. While the coherent Rabi oscillations were undoubtedly found responsible for the observed pulse breakup at high input energies in the gain regime, the focusing action of the linear dispersion combined with the Kerr effect was essential for producing key features such as: (i) at transparency, "soliton-like" propagation and pulse narrowing at high intensities as observed in the experiments, (ii) in the gain regime, constraining the pulse breakup and clamping of the peak intensity, as well as the reproduction of two equally deep redshifts which cannot be reconstructed otherwise, and (iii) in the absorption regime, the redshifts observed in the experiments were predicted only by the action of the Kerr effect.

Conclusively, this investigation provides a better understanding of the mechanisms that shape the pulse while propagating in the SOA, and will serve to predict and delineate more accurately the result of future experiments.

ACKNOWLEDGMENTS

This work was partially supported by the Israeli Science Foundation. A.K.M. is thankful for the financial support from the PBC Fellowship. O.K. is thankful for the financial support provided during this research from the Daniel Fellowship, and from the Russel Berrie Institute.

[1] A. Capua, O. Karni, G. Eisenstein, and J. P. Reithmaier, Phys. Rev. B **90**, 045305 (2014).

[2] O. Karni, A. Capua, G. Eisenstein, V. Sichkovskyi, V. Ivanov, and J. P. Reithmaier, Opt. Express **21**, 26786 (2013).

[3] M. Kolarczik, N. Owschimikow, J. Korn, B. Lingnau, Y. Kaptan, D. Bimberg, E. Schöll, K. Lüdge, and U. Woggon, Nat. Commun. **4**, 2953 (2013).

[4] R. W. Ziolkowski, J. M. Arnold, and D. M. Gogny, Phys, Rev. A **52**, 3082 (1995).

[5] A. Capua, O. Karni, and G. Eisenstein, IEEE J. Select. Top. Quantum Electron. **19**, 1900410 (2013).

[6] A. Capua, G. Eisenstein, and J. P. Reithmaier, Appl. Phys. Lett. **97**, 131108 (2010).

[7] P. Lunnemann, S. Ek, K. Yvind, R. Piron, and J. Mørk, New J. Phys. **14**, 013042 (2012).
[8] P. Borri, W. Langbein, J. M. Hvam, F. Heinrichsdorff, M.-H. Mao, and D. Bimberg, IEEE Photonics Technol. Lett. **12**, 594 (2000).
[9] O. Karni, K. J. Kuchar, A. Capua, V. Mikhelashvili, G. Sęk, J. Misiewicz, V. Ivanov, J. P. Reithmaier, and G. Eisenstein, Appl. Phys. Lett. **104**, 121104 (2014).
[10] A. J. Zilkie *et al.*, IEEE J. Lightwave Technol. **26**, 1498 (2008).
[11] T. H. Siederdissen, N. C. Nielsen, and J. Kuhl, J. Opt. Soc. Am. B **23**, 1360 (2006).
[12] M. Bagnell, J. Davila-Rodriguez, A. Ardey, and P. J. Delfyett, Appl. Phys. Lett. **96**, 211907 (2010).
[13] F. Romstad, P. Borri, W. Langbein, J. Mørk, and J. M. Hvam, IEEE Photonics Technol. Lett. **12**, 1674 (2000).
[14] A. Knorr and S. Hughes, IEEE Photonics Technol. Lett. **13**, 782 (2001).
[15] S. Hughes, P. Borri, A. Knorr, F. Romstad, and J. M. Hvam, IEEE J. Select. Top. Quantum Electron. **7**, 694 (2001).
[16] J. Zhang and I. Galbraith, IEEE J. Quantum Electron. **41**, 1083 (2005).
[17] R. Trebino, *Frequency-Resolved Optical Gating: The Measurement of Ultrashort Laser Pulses* (Kluwer Academic, Norwell, MA, 2002).
[18] C. Gilfert, V. Ivanov, N. Oehl, M. Yacob, and J. P. Reithmaier, Appl. Phys. Lett. **98**, 201102 (2011).
[19] R. M. Joseph and A. Taflove, IEEE Trans. Antennas Propag. **45**, 364 (1997).
[20] N. Suzuki, IEEE J. Lightwave Technol. **25**, 2495 (2007).
[21] P. Y. Yu and M. Cardona, *Fundamentals of Semiconductors* (Springer, Berlin, 2003).
[22] R. Wang, X. Sheng, Y. Mao, Z. Zhu, C. Wu, and H. Dong, Infrared Phys. Technol. **67**, 155 (2014).